Eurasian Journal of Physics and Functional Materials

2026, 10(4), 368-375

High-Entropy Double Manganite $(Y_{0.2}Dy_{0.2}Nd_{0.2}Pr_{0.2}La_{0.2})BaMn_2O_6$

E.V. Sterkhov, L.B. Vedmid', S.G. Titova*

Vatolin Institute of Metallurgy UB RAS, Yekaterinburg, Russia

E-mail: sgtitova@mail.ru

DOI: **10.32523/ejpfm.2026100403**
Received: 27 August 2026
Revised: 01 November 2026
Accepted: 14 November 2026

Structure and physical properties (magnetization, electrical resistivity, heat capacity) for high-entropy double manganite $(Y_{0.2}Dy_{0.2}Nd_{0.2}Pr_{0.2}La_{0.2})BaMn_2O_6$ are studied for the first time. The resistance is almost independent of the magnetic field up to 3 *T*. A comparison with $Nd_{0.6}Sm_{0.4}BaMn_2O_6$ solid solution having an equal average ionic radius of the *R* -elements allows extraction of the high-entropy state effect: an increase of the metal-insulator transition temperature and a suppression of the magnetic order in Mn-subsystem.

Keywords: high-entropy compound, double manganite, crystal structure, electrical resistivity, magnetic properties.

1. Introduction

High-entropy alloys have attracted much attention over the last twenty years [1–3], demonstrating a promising route to creating a new class of materials containing multiple elements in equiatomic concentrations. This approach yields new alloys with high stability and functional properties. Recently, oxide materials with multi-component substitution in $A_2B_2O_7$, AO, A_2O_3, and $AB_{12}O_{19}$ oxides have been studied [4–7]. Moreover, for the high-temperature superconducting oxide $RBa_2Cu_3O_7$ with five different rare-earth elements at the R-site, an increased critical current was observed [8]. High-entropy polycrystalline manganites of rare-earth elements have demonstrated a colossal magnetoresistance effect of $\sim$1550 % in the vicinity of the metal–insulator transition (MIT) [9].

So-called double or ordered manganites $RBaMn_2O_6$ (R = rare-earth element) consist of alternating layers of $RMnO_3$ and $BaMnO_3$ with an almost cubic perovskite structure, forming a tetragonal or orthorhombic structure with $a \approx a_p \approx b_p$ and $c \approx 2c_p$, where the subscript p denotes the unit cell of a simple cubic perovskite [10]. Double manganites exhibit a rich phase diagram when the R-element varies [11–16]. These materials are bad metals at high temperatures; upon cooling, the MIT occurs due to charge or orbital ordering in the Mn sublattice. At low temperatures, double manganites contain both ferromagnetic and antiferromagnetic phases (or clusters) [17, 18]. The materials with R = Pr and La have Curie temperatures T_C of ~ 303 K and ~ 330 K, respectively [10]. Evidently, the choice of the R-element determines the magnetic order type and the MIT temperature. As well as disordered manganites $RMnO_3$, double manganites $RBaMn_2O_6$ demonstrate an influence of the magnetic field on the electrical resistivity (magnetoresistance); a presence of magnetic phase transitions near room temperature makes them attractive magnetocaloric materials [19].

The ground state for double manganites with R = Pr, La is a mixture of antiferromagnetic insulator and ferromagnetic metal states. Moreover, A-type of antiferromagnetic phase reveals metallic behavior while CE-type is insulator; the energies of these states are very close [20]. The defects, the stoichiometry and the disorder provide a favor for the metallic or the insulating state [20]. Indeed, substitution of Ba by smaller Sr and Ca ions reduces the mismatch between R- and Ba-ions and introduces the structural disorder in Ba-site; this leads to suppression of either the charge/orbital insulating state or the A-type antiferromagnetic state for double manganites with R = Nd, Pr, $Nd_{0.5}Sm_{0.5}$ [21]. The randomness effect caused by a mixture of R-ions with different ionic radius while R and Ba atoms regularly ordered to form the double manganite structure was studied in refs. [22–24]. It was found that such a mixture may provide strong phase separation tendencies among ferromagnetic, antiferromagnetic and charge/orbital ordered insulating states and lead to the large magnetoresistance [19, 22, 25].

In this paper, we synthesized single-phase polycrystalline high-entropy manganite $(Y_{0.2}Dy_{0.2}Nd_{0.2}Pr_{0.2}La_{0.2})BaMn_2O_6$ (YDNPL) and investigated its structure and physical properties. The ratio $r(R)/r(\mathrm{Ba}) = 0.78$ for this material, where $r(R)$ is the average ionic radius of the R-elements and $r(\mathrm{Ba})$ is the ionic radius of barium [26]. This ratio corresponds to the $Nd_{1-x}Sm_xBaMn_2O_6$ solid solution with a samarium content $x \approx 0.4$ studied earlier [13]; this allows a comparison between high-entropy compound and simpler one. The $Nd_{0.6}Sm_{0.4}BaMn_2O_6$ (N6S4) solid solution demonstrates two phase transitions with different types of Mn^{3+}/Mn^{4+} charge ordering at 336 K and at 205 K. The high-temperature transition is linked to the MIT. The N6S4 compound also exhibits a Néel temperature $T_N = 124$ K. We compare the high-entropy manganite (YDNPL) and the N6S4 solid solution, which have equal average ionic radii of the R-elements, to extract the effect of the high-entropy state.

2. Materials and methods

The samples were obtained by citrate-nitrate method using R_2O_3 (R = Y, Dy, Nd, La), Pr_4O_{11}, Mn_2O_3, and $BaCO_3$ as starting materials. The stoichiometric quantities were dissolved for 2 hours in boiling nitric acid; the resulting solution was then subjected to pyrolysis at 200–250 °C using citric acid. The resulting powder was pressed into pellets and treated at 1100 °C in air for 12 hours to obtain the single-phase disordered $R_{0.5}Ba_{0.5}MnO_3$ oxide. In the next step, thermal treatment at 1100 °C for 24 hours at low partial oxygen pressure $\lg P_{O_2}$ (atm.) = -19, with intermediate grindings, was performed to synthesize the ordered $RBaMn_2O_{6-\delta}$ manganite. At the final stage, the oxygen vacancies were removed by oxidation at 300–500 °C for 12 hours in a pure oxygen flow [13].

The chemical composition was examined by a Carl Zeiss EVO 40 scanning electron microscope equipped with an INCA X-Act energy-dispersive X-ray analyzer. Heat capacity data (C_p) data were measured using a DSC 214 Polyma (NETZSCH) calorimeter, as described previously [13].

X-ray powder diffraction (XPD) was carried out using a Shimadzu XRD-7000 diffractometer (Cu Kα radiation, graphite monochromator). An Anton Paar TTK 450 chamber with liquid nitrogen was used for low-temperature measurements upon heating. The crystal structure was refined by Rietveld analysis using the FullProf package [27].

A four-probe technique was used for the electrical property measurements. The K2400 SourceMeter (Keithley) was used as a current source; the voltage was measured by K2182 nanovolt-meter (Keithley). The indium-gallium paste was used for electrical contacts; the contacts were soldered to the measuring cell using a pure indium. Magnetic properties were studied using a Cryogenic CFS-9T-CVTI magnetometer in the temperature range of 4–320 K. At higher temperatures, up to 400 K, the Faraday balance method was used. Magnetization as a function of temperature was measured using the standard zero-field-cooled (ZFC) and field-cooled (FC) procedure with a magnetic field 0.01 T. The magnetic moment per formula unit M was determined, and isothermal magnetization $M(B)$ was obtained in magnetic fields up to ± 5 T.

3. Results and Discussion

Obtained ceramic samples have dense structure, the average grain size ~ 5 μm (Figure 1). According to the EDS analysis (Figure 2 and Table 1), all rare-earth elements exhibit a uniform and homogeneous distribution, as do the other components, and the relative chemical quantities match the general formula. At room temperature, the crystal structure is tetragonal with the *P4/mmm* space group. Figure 3 (a) shows the experimental, calculated, and difference diffraction patterns. The obtained structural parameters and discrepancy factors are listed in Table 2. The lattice parameters and unit cell volume for the YDNPL and N6S4 compounds are the same within statistical deviation, as a result of the similar average radius of rare-earth elements.

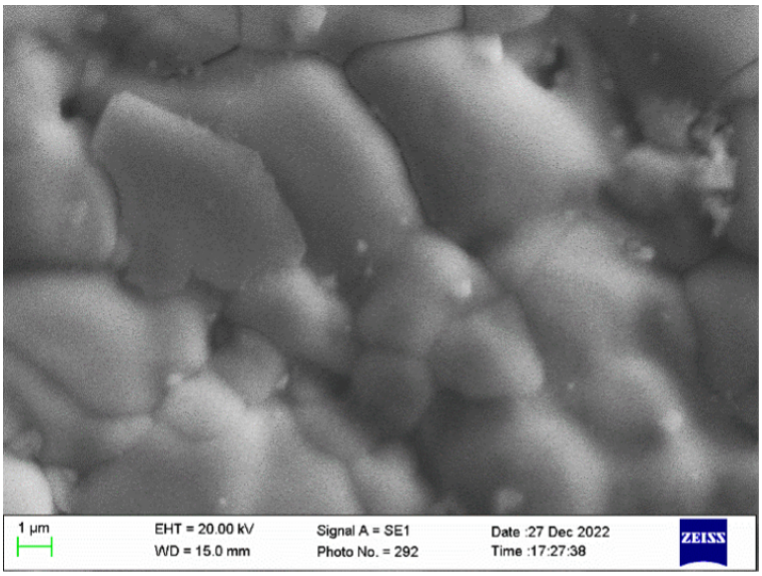


Figure 1. SEM image of ceramic $(Y_{0.2}Dy_{0.2}Nd_{0.2}Pr_{0.2}La_{0.2})BaMn_2O_6$ (YDNPL) sample.

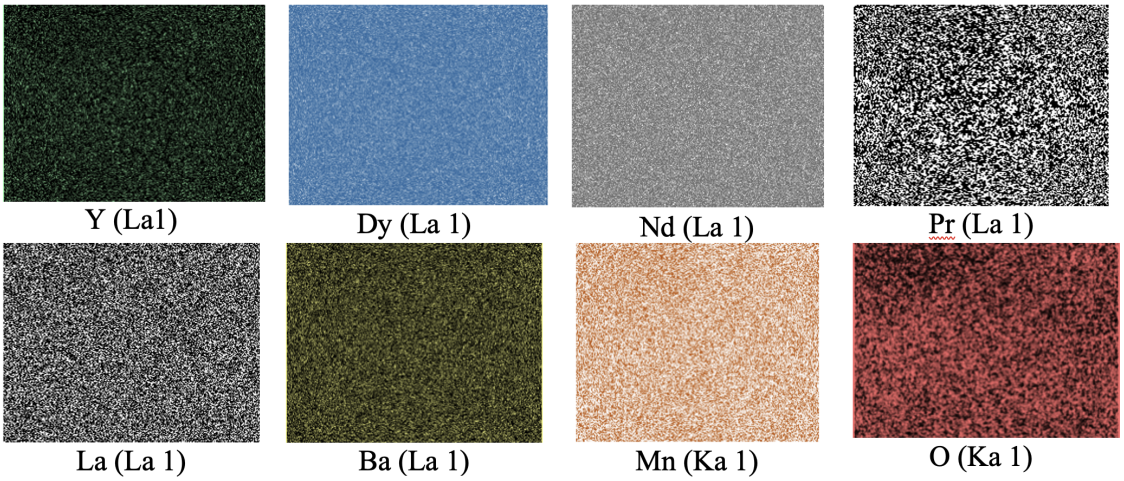


Figure 2. Element distribution maps and resulting chemical composition for YDNPL sample.

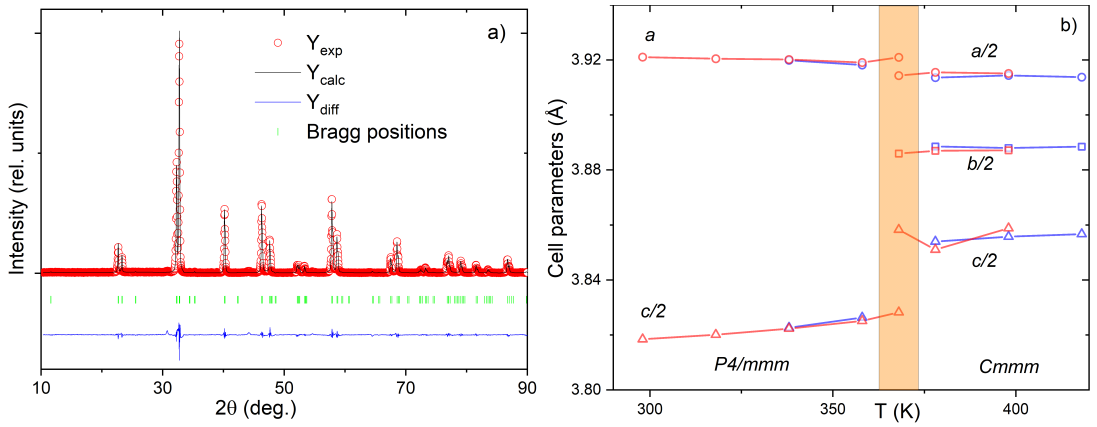


Figure 3. The XPD spectrum for YDNPL sample: experimental, calculated and difference diffraction patterns at room temperature (a), thermal evolution of the unit cell parameters during heating (red lines and symbols) and cooling (blue lines and symbols). The orange shaded area indicates the two-phase region (b).

Table 1. EDS analysis results for YDNPL sample.

Element	Y	Dy	Nd	Pr	La	Ba	Mn
Quantity, rel. at. %	2.0	2.3	2.2	2.1	3.0	11.9	19.5

Table 2. Structural parameters for YDNPL at room temperature (*P4/mmm* space group).

Parameter	$(Y_{0.2}Dy_{0.2}Nd_{0.2}Pr_{0.2}La_{0.2})BaMn_2O_6$
a, Å	3.92107(3)
c, Å	7.63688(8)
V, Å^3	117.415(2)
z(Mn)	0.244(1)
z(O2)	0.235(3)
R_{wp}, %	16.4
R_{exp}, %	7.57
R_p, %	11.5
R_B, %	7.85

The MIT for double manganites is associated with a change of the a/c ratio; the transition to the insulating state is related to the contraction of c-parameter and the elongation in the (ab)-plane [28, 29]. At room temperature, the ratio $2a/c = 1.027$ (from Table 2); this indicates that the MIT for the YDNPL compound occurs above room temperature. The significant deviation of the O2-Mn-O2 bond angle (176.2°) from 180° also confirms the insulating state. *In-situ* diffraction analysis reveals a structural phase transition at the MIT, which occurs at $T_{MIT} \sim 368$ K upon heating, see Figure 3 (b). The transition is first-order, with a wide two-phase region of about 20 K. The T_{MIT} for the high-entropy YDNPL compound is higher than that for the N6S4 solid solution $T_{MIT} \sim 336$ K [13].

The electrical and magnetic properties of YDNPL are shown in Figures 4 and 5. The electrical resistivity below the MIT exhibits activation-type behavior and weakly depends on the magnetic field up to 3 T (Figure 4). The temperature and field dependences of the magnetization for the (YDNPL) compound are shown in Figure 5.

The MIT temperature is clearly visible as a sharp peak in the heat capacity in Figure 5(a), and its position is in a good agreement with the structural phase transition in Figure 3(b). Below the MIT, a slight drop in magnetization occurs. The increased magnetization above the MIT is possibly due to weak ferromagnetic interactions in the metallic state.

Almost linear field dependences $M(B)$ are observed in the temperature range of 20–315 K (Figure 4(b)), indicating that the sample remains almost paramagnetic below the MIT. Only at 4 K there is a sign of magnetic ordering, possibly due to interactions in the rare-earth sublattice. The temperature dependence of the magnetization measured at 0.01 T (Figure 5(a)) reveals rather small magnetic moment per formula unit, which is typical for the paramagnetic state. A broad maximum is also observed near 200 K. A similar magnetization maximum was

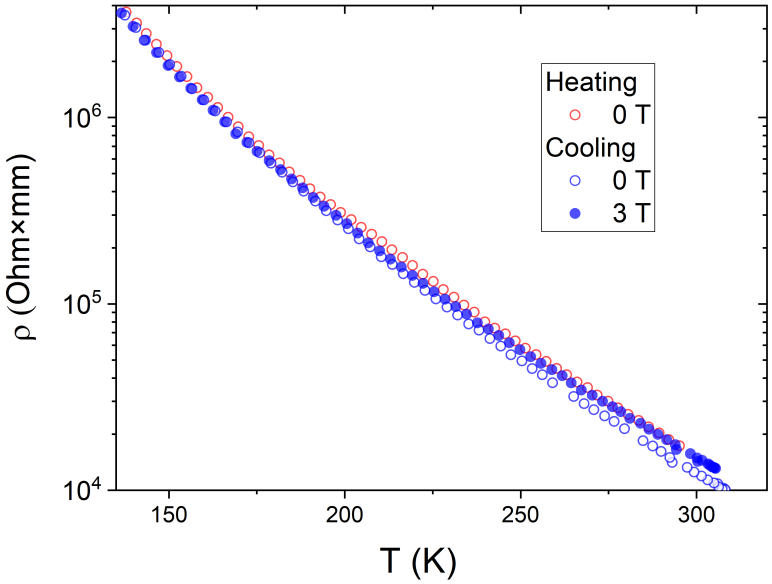


Figure 4. Electrical resistivity for YDNPL as a function of temperature in magnetic field 0 and 3 T.

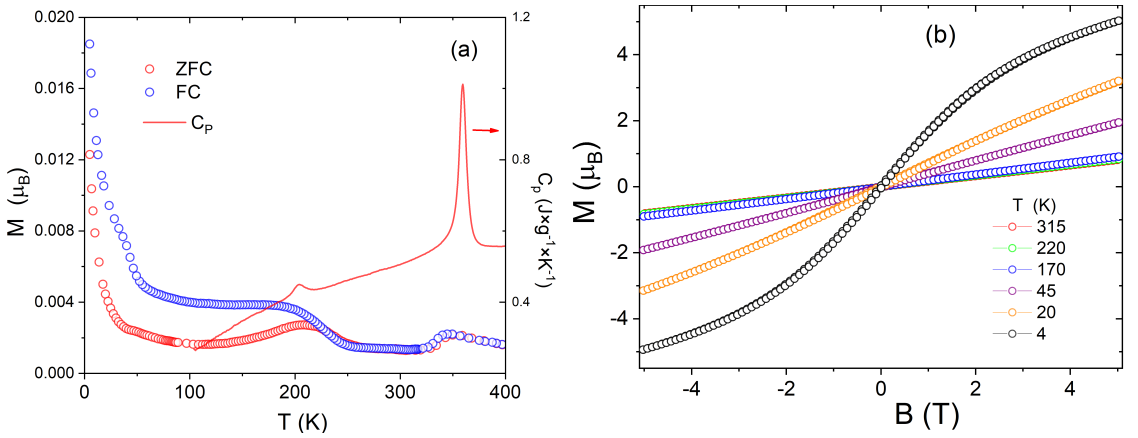


Figure 5. Heat capacity C_p and magnetization M per formula unit as a function of temperature (a) and magnetization M per formula unit as a function of magnetic field (b) for YDNPL sample.

reported earlier for ceramic samples [29, 30] but was absent in high-quality single crystals [15]. This maximum was attributed to grain boundary effects [31]. As noted above, the simpler N6S4 compound becomes antiferromagnetic below $T_N = 124$ K. In conclusion, the high-entropy state increases the MIT temperature and suppresses magnetic ordering in the Mn-sublattice.

4. Conclusion

We have compared two ordered (double) manganites: the high-entropy composition $(Y_{0.2}Dy_{0.2}Nd_{0.2}Pr_{0.2}La_{0.2})BaMn_2O_6$ (YDNPL) and $Nd_{0.6}Sm_{0.4}BaMn_2O_6$ (N6S4) solid solution, both having the same average ionic radius of the R-elements. Crystal structure and unit cell parameters for both materials coincide but the properties are different. First, YDNPL exhibits a higher metal–insulator

transition (MIT) temperature (368 *K* for YDNPL vs. 336 *K* for N6S4). Second, the high-entropy state suppresses antiferromagnetic ordering in the Mn-sublattice: YDNPL remains paramagnetic down to 4 *K*, whereas N6S4 becomes antiferromagnetic below 124 *K*. The latter observation is not surprising, as lattice disorder caused by a mixture of different rare-earth ions is expected to lower the magnetic ordering temperature. Suppression of both antiferromagnetic and charge/orbital order caused by disorder in the A-site of the perovskite structure occupied by either *R* or Ba ions was reported earlier for double manganites [21–23], but no effect of such a disorder on Curie temperature was found [24]. To verify this fact, the study of the high-entropy material with larger average *R*-ion radius is required. To explain the first observation, we note that the MIT is a first-order phase transition. Possibly, the presence of different local environments for the MnO_6 octahedra gives rise to low-temperature transition centers. As a consequence, the two-phase coexistence region is broadened. Obtained results are important to understand the properties of manganites and double manganites of rare earth elements.

Acknowledgments

Magnetic and electrical properties were investigated at collective usage center Ural-M in IMET UB RAS. The study was supported by RSF, project No. 25-23-00102 (https://rscf.ru/project/25-23-00102/).

References

[1] J.-W. Yeh et al., Adv. Eng. Mater. **6** (2004) 299–303. [*CrossRef*]
[2] B. Cantor et al., Mater. Sci. Eng. A **375–377** (2004) 213–218. [*CrossRef*]
[3] E.P. George et al., Nat. Rev. Mater. **4** (2019) 515–534. [*CrossRef*]
[4] Z. Teng et al., J. Eur. Ceram. Soc. **40** (2020) 1639–1643. [*CrossRef*]
[5] Z. Grzesik et al., J. Eur. Ceram. Soc. **40** (2020) 835–839. [*CrossRef*]
[6] D.A. Vinnik et al., Ceram. Int. **45** (2019) 12942–12948. [*CrossRef*]
[7] K.-P. Tseng et al., J. Am. Ceram. Soc. **103** (2019) 569–576. [*CrossRef*]
[8] S. Pryanichnikov et al., J. Supercond. Novel Magn. **36** (2023) 871–875. [*CrossRef*]
[9] A. Sarkar et al., Adv. Mater. **35** (2022) 2207436. [*CrossRef*]
[10] T. Nakajima et al., J. Phys. Soc. Jpn. **72** (2003) 3237–3242. [*CrossRef*]
[11] Y. Ueda et al., J. Phys.: Condens. Matter **16** (2004) S573–S583. [*CrossRef*]
[12] S.G. Titova et al., J. Supercond. Novel Magn. **33** (2020) 1899–1903. [*CrossRef*]
[13] E.V. Sterkhov et al., Mater. Today Commun. **34** (2023) 105005. [*CrossRef*]
[14] T. Nakajima et al., Physica B **329–333** (2003) 844–845. [*CrossRef*]
[15] S. Yamada et al., J. Solid State Chem. **315** (2022) 123504. [*CrossRef*]
[16] D. Akahoshi et al., Phys. Rev. B **70** (2004) 064418. [*CrossRef*]
[17] Y. Kawasaki et al., Phys. Rev. Lett. **96** (2006) 037202. [*CrossRef*]
[18] Y. Kawasaki et al., Phys. Rev. B **86** (2012) 125141. [*CrossRef*]
[19] A.M. Aliev et al., J. Alloys Compd. **509** (2011) L165–L167. [*CrossRef*]

[20] S.V. Streltsov et al., J. Alloys Compd. **912** (2022) 165150. [*CrossRef*]
[21] D. Akahoshi et al., J. Solid State Chem. **228** (2015) 105–109. [*CrossRef*]
[22] Y. Miyauchi et al., J. Phys.: Conf. Ser. **200** (2010) 012123. [*CrossRef*]
[23] Q. Gao et al., Chin. Phys. B **22** (2013) 077502. [*CrossRef*]
[24] S.G. Titova et al., Solid State Commun. **419** (2027) 116650. [*CrossRef*]
[25] N.N. Loshkareva et al., Phys. Solid State **44** (2002) 1916–1924. [*CrossRef*]
[26] Y.Q. Jia, J. Solid State Chem. **95** (1991) 184–187. [*CrossRef*]
[27] J. Rodríguez-Carvajal, Physica B **192** (1993) 55–69. [*CrossRef*]
[28] J. Blasco et al., Phys. Rev. B **103** (2021) 064105. [*CrossRef*]
[29] E.V. Sterkhov et al., J. Alloys Compd. **892** (2022) 162034. [*CrossRef*]
[30] J. Blasco et al., Phys. Rev. B **103** (2021) 214110. [*CrossRef*]
[31] S. Yamada et al., J. Phys. Soc. Jpn. **81** (2012) 113711. [*CrossRef*]